공학석사 학위논문

Study on lens design methods for improving the viewing properties of the integral imaging system degraded by lens-array aberrations

렌즈 어레이의 수차에 의하여 저하되는 집적 영상의 시야 특성을 향상시키는 렌즈 디자인에 대한 연구

2015 년 7 월

서울대학교 대학원
전기 컴퓨터 공학부
Matheus Farias Miranda

Study on lens design methods for improving the viewing properties of the integral imaging system degraded by lens-array aberrations

렌즈 어레이의 수차에 의하여 저하되는 집적 영상의 시야 특성을 향상시키는 렌즈 디자인에 대한 연구

지도 교수 이병호

이 논문을 공학석사 학위논문으로 제출함

2015 년 7 월

서울대학교 대학원

전기 컴퓨터 공학부

Matheus Farias Miranda

Matheus Farias Miranda 의 공학석사 학위논문을 인준함

2015 년 7 월

위 원 장 _____ (인)

부위원장 _____ (인)

위 원 _____ (인)

ABSTRACT

Integral imaging (InIm) is a promising three-dimension (3D) display technique because it can display 3D images with vertical and horizontal parallax without the need for any special glasses. InIm requires a lens-array in front of the display panel in order to integrate the elemental images (EI) into the 3D image. Conventionally the elemental lenses have spherical surface profiles, thus they suffer from intrinsic lens aberrations such as spherical aberration and astigmatism. Aberrations affect the ability of the lens to focus light in a single point, or to collimate light from a point source. In InIm, this results in a loss of image quality of the elemental images and reconstructed image due to distortions. The viewing characteristics of the InIm system, such as viewing angle and image resolution, are also affected by aberrations.

In this work the author proposes two methods designing aberration-minimized lens-array. The first method is based on the splitting and bending of the lens-array's elemental lens such that aberration balancing can be achieved. Simulations are performed and the effectiveness of this method is demonstrated by comparing the designed lens-array with a standard spherical lens-array of same properties. In the second method the author describes the design process of a custom aspherical lens-array which has minimum spherical aberration. The design, optimization, and fabrication processes are described. Experiments are presented and compared with the computer simulations. A thorough analysis of the results is performed and solutions to the issues encountered are proposed.

Keywords: Integral imaging, lens design, aberrations, three-dimensional display.

Student number: 2013-23844

TABLE OF CONTENTS

LIST OF FIGURES

LIST OF TABLES

1 INTRODUCTION

The integral imaging (InIm) is a technique that can record and reconstruct the light field of a scene by using a lens-array to spatially sample the light rays from different perspectives and then displaying this information through another lens-array. Due to the fact that the recorded image through the lens-array (called elemental images, or EIs) contains both the intensity and angular information of the scene, when the EIs are displayed by a flat panel or projector and imaged again by the lens-array, the light field is reconstructed and the EIs integrate forming a three-dimensional (3D) image. This is a very promising technique because the apparatus required is relatively simple and it can provide full parallax without the need for any special glasses [1]–[3]. However, both the pickup and display stages require a lens-array (or micro lens-array) and just like any lens, they suffer from intrinsic lens aberrations such as spherical, coma, astigmatism, Petzval field curvature, and distortion. Though small, aberrations affect the quality of the reconstructed 3D images and also degrade the viewing characteristics of the InIm system, therefore they should be considered in the InIm system design and minimized as much as possible.

InIm was proposed in 1908 by Lippman [4] and since then a lot of research has been done aiming to improve the properties of the InIm system. The resolution of the EI, the elemental lens pitch, and elemental lens surface profile are some of the factors that affect the quality of the reconstructed image. Techniques have been suggested to improve the InIm image resolution and viewing angle [5], [6]. However, not as much research has been done on the effect of the shape of the elemental lens on the image quality and viewing characteristics of the InIm. In this paper the author

proposes a method to design an aspherical lens-array and a quartet lens-array that can improve the quality of the EI and reconstruct 3D image by minimizing the aberrations.

1.1 Integral imaging

Integral imaging is based on the capture and reproduction of the light field of an object or scene. The advantage of using the light field is that it contains both the intensity and directional information of the light rays coming from the object. The captured information can be used to generate a depth map of the object, reconstruct the 3D image or display the 2D image with different depth focus. The latter is one of the features of the light field camera commercialized by Lytro [7]. Recording the elemental images through the two-dimension lens-array is similar to taking many pictures of the same object from different perspectives. With that information it is possible to use disparity algorithms to extract the depth map. MIT Media Labs uses this concept to extract the depth map from a pinhole array [8]. In this work the author will focus only on the EI acquisition and 3D image reconstruction, i.e.: InIm pickup and display.

The main disadvantages of the light field display are that it has reduced resolution and restricted viewing angle compared to standard 2D display.

1.1.1 Principle of integral imaging

InIm is separated into two parts: pickup and display. As shown in Fig. 1, the setup used for the pickup stage is usually a 2D lens-array, or micro lens-array, and a recording device, usually a camera with a CCD or a CMOS image sensor. At the image plane, this setup provides a set of equally spaced 2D elemental images, each

having information of a different perspective of the object. This is actually equivalent to moving a camera and taking a picture at each lens position or having an array of cameras instead of an array of lenses. The problem with using a lens-array is that it has fixed focal length, hence only one plane of the object space (reference plane in figure) is in focus at the camera plane. The light emitted by points of the object which are out of the imaging plane does not focus onto the CCD and therefore gives rise to blurred images. The blur increases with distance from the imaging plane. Apart from the limited depth of field (DOF), InIm pickup stage is also limited by the overlapping of EI, which happens when the portion of the object imaged by an elemental lens is recorded on the CCD pixels which correspond to the adjacent elemental lens. Consequently this also limits the viewing angle. Figure 1 illustrates the pickup stage, where ρ is the elemental lens pitch, g is the distance between the camera plane and the lens-array, and l is the distance between the lens-array and the reference plane.

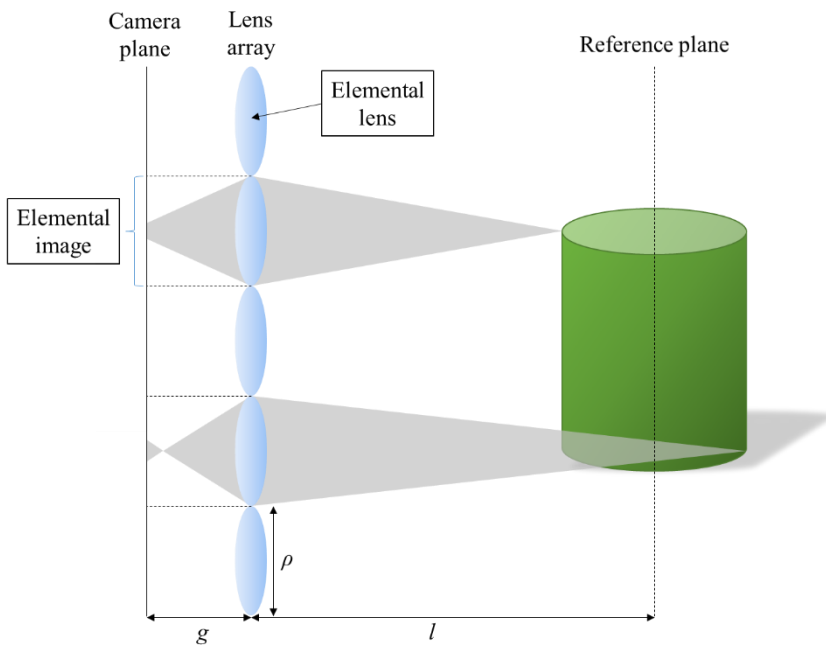

Figure 1: Diagram representation of the pickup stage of the InIm system.

In the display stage the properly processed EI is displayed on a display panel (usually a liquid crystal display (LCD)) placed in front of a similar lens-array. Now the rays emitted by the points in the EI refract in the lens-array and integrate at the respective image points, such that the 3D scene is reconstructed. It is important to point out that the observer will only perceive depth if the two eyes receive light from the reconstructed points. An issue with the display stage is the limited resolution of the display panel, which can compromise the lateral and depth resolution of the reconstructed scene. Advances in display technology are reducing the impact of this problem. Another problem is, due to the imaging properties of the lenses, only the points on the imaging plane (also referred to as central depth plane (CDP)) are reconstructed sharply. As illustrated in Fig. 2, this happens because the light beams from each elemental lens converge at the CDP (assuming ideal lenses) and although

depth can be perceived around the CDP, other parts of the 3D object are increasingly blurred. Regarding the image quality and integrity of the reconstructed images, there are two important aspects in InIm display: pseudoscopic to orthoscopic conversion and discontinuity due to multifacet structure [9]. The former deals with the inverted depth problem in InIm. This problem can be solved optically [10] or by modifying the EI using image processing software [11].

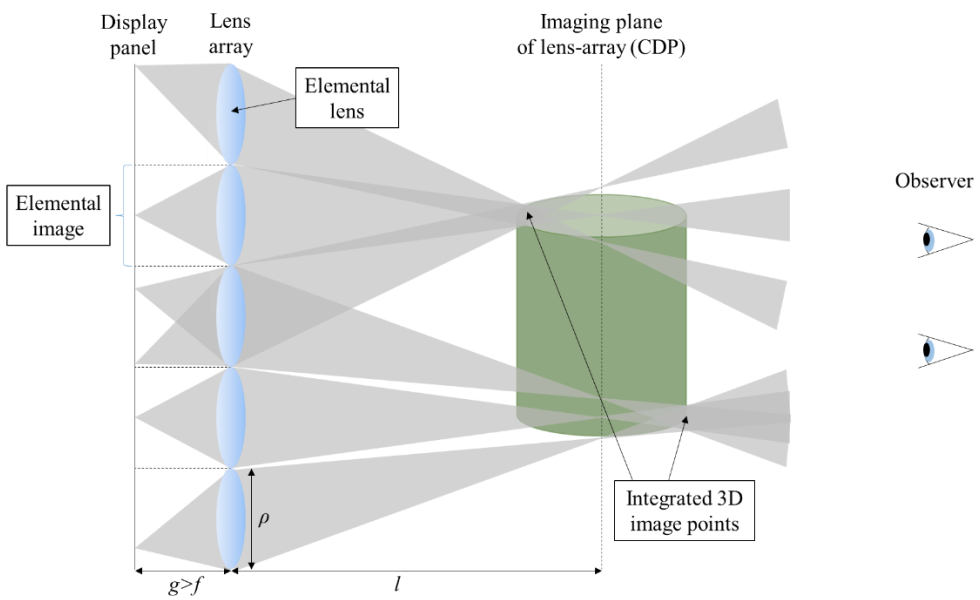

Figure 2: Diagram representation of the display stage of the InIm system (Real mode).

InIm display has three possible modes: real, virtual and focal mode. The mode is mostly defined by the gap between the display panel and the lens-array. Figure 2 illustrates the real mode, where the gap is larger than the focal length of the elemental lens, therefore according to the lens equation, Eq. (1), the CDP is located on the viewer side of the lens.

$$\frac{1}{f}=\frac{1}{g}+\frac{1}{l} \quad . \tag{1}$$

Figure 3 illustrastes the virtual mode, where the gap is smaller than the focal length and consequently the CDP is located behind the lens array. The last case is the focal mode. As the name implies, in this mode the gap is set to equal to the focal length. The CDP in this case is located at infinity, hence the light rays are collimated and do not have a focal point like the other modes. Focal mode is illustrated in Fig. 4.

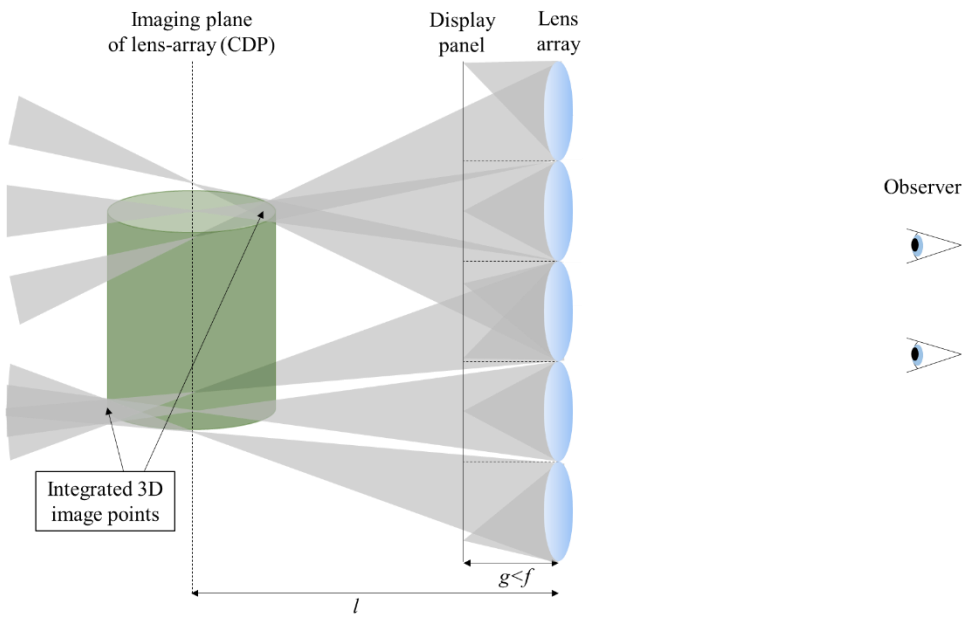

Figure 3: Diagram representation of the display stage of the InIm system (Virtual mode).

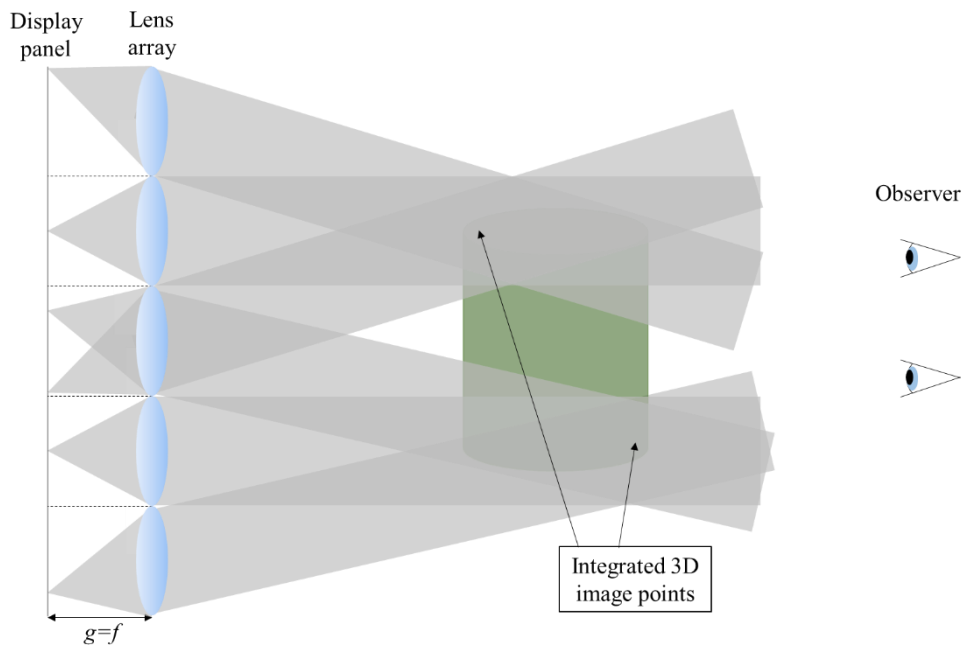

Figure 4: Diagram representation of the display stage of the InIm system (Focal mode).

Each mode has advantages and disadvantages, real mode for example generates 3D images closer to the observer, creating a pop-out effect. On the other hand in focal mode the resolution is equal to the number of elemental lenses and the number of pixels under each elemental lens is equal to the resolution of the sub-image.

1.1.2 Viewing characteristics of integral imaging

The viewing characteristics of an InIm system are the image resolution, the image depth and the viewing angle. All of which can be defined by the parameters of the system such as lens pitch, gap, and display resolution. Equations (2)-(5) are known as the characteristic equations. Figures 5 and 6 illustrate the viewing parameters of the InIm system.

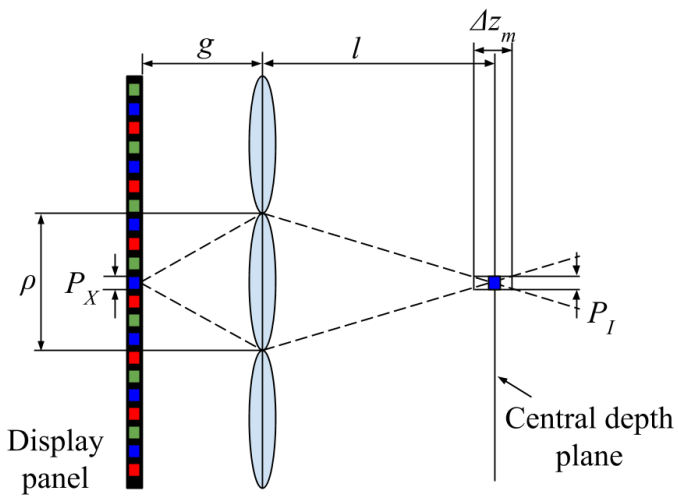

Figure 5: Definition of image depth and resolution.

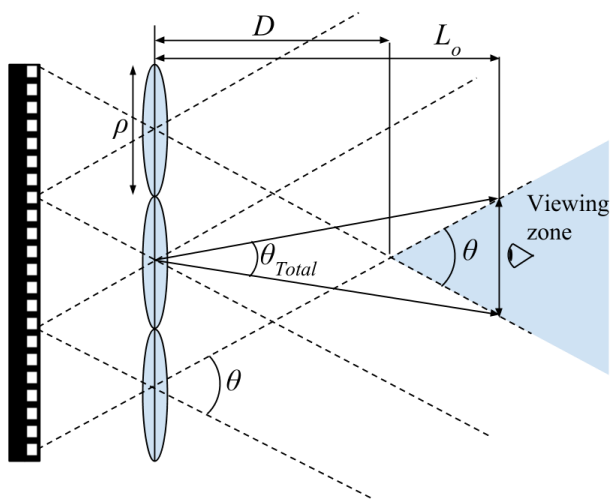

Figure 6: Definition of the viewing angle.

The characteristic equations are

$$R_I = \frac{1}{P_I} = \frac{g}{lP_x} \quad , \tag{2}$$

$$\Delta z_m = 2\frac{l}{\rho}P_I \quad , \tag{3}$$

$$\theta_{total\_real} = 2\arctan\left\{\frac{\rho\left[lL_o - (N-2)lf - 2fL_o\right]}{2lfL_o}\right\}, \tag{4}$$

and

$$\theta_{total\_virtual} = 2\arctan\left[\frac{\rho(L_o - Nf)}{2fL_o}\right], \tag{5}$$

where, P_x is the display pixel pitch, R_I is the image resolution, Δz_m is the image depth, θ is the viewing angle, ρ is the lens pitch, g is the gap, l is the distance from the lens-array to the CDP, L_o is the distance from the lens-array to the viewer, and N is the number of elemental lens involved in displaying the image [12], [13].

1.2 Seidel aberrations

Aberrations are present in all kinds of lenses and the distortions caused by them depend on the type and severity of the aberration. In this paper the author will focus on monochromatic aberrations because the materials considered in this work have low chromatic dispersion ($dn/d\lambda$ = -0.0096160 μm^{-1}) and according to our simulations chromatic aberration has negligible effect on the image quality (focal shift of ± 0.1 mm). In general, aberrations affect the ability of the lens to focus light on a single point, or to collimate light from a point source, therefore compromising the imaging properties of the lens.

The five main monochromatic aberrations, also known as Seidel aberrations are: spherical aberration, coma, astigmatism, field curvature and distortion [15]. Spherical aberration happens due to the higher refraction of light rays striking the edge of the lens compared to the paraxial rays (near the center). This often causes the edge (or marginal) rays to cross the optical axis before the paraxial rays do, thus difference of focal points exists. Coma can be described as a variation in magnification over the entrance pupil which causes parallel off-axis light rays, such as the ones coming from a star, to appear distorted. The distortion observed resembles a comet, hence the name. Astigmatism is the aberration that causes the lens to have a sagittal focus and a tangential focus, or in other words, rays propagating in two perpendicular planes have different focus. Field curvature, also known as Petzval field curvature, is the aberration in which a flat object is imaged by the lens onto a curved (image) plane. Lastly, distortion is the aberration in which straight lines in a scene are not imaged as straight lines. There are three types of radial distortion: Barrel, pincushion and mustache distortion.

In this thesis, the five monochromatic aberration will be quantified in terms of wavefront aberration coefficient. The physical meaning of these aberration coefficients is the peak-to-valley optical path difference (OPD) between the aberrated wavefront and the reference (ideal) wavefront at the edge of the exit pupil of the system, as shown in Fig. 7. Figure 8 shows a 3D diagram of the wavefront aberration caused by spherical aberration and how the spherical aberration coefficient is measured.

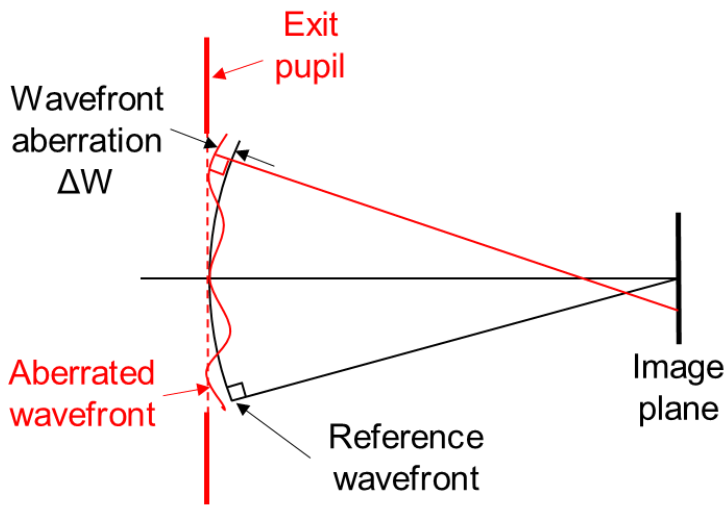

Figure 7: Definition of wavefront aberration.

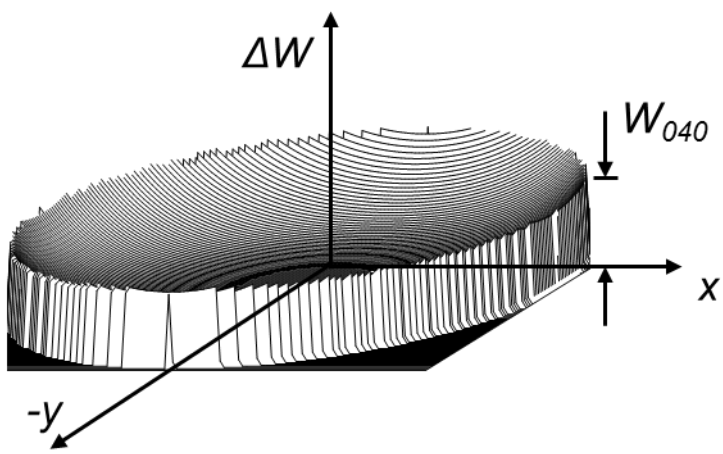

Figure 8: 3D diagram of spherical aberration of wavefront.

In Eq. (6), W is the wavefront aberration coefficient while S is the Seidel aberration coefficient. S_I is the spherical aberration, S_{II} is the coma aberration, S_{III} is the astigmatism, S_{IV} is the field curvature, and S_V is the distortion. Wavefront and Seidel coefficients are closely related and can be calculated in micrometers and waves.

$$W_{040} = \frac{1}{8} S_I = -\frac{1}{8} \sum A^2 y \Delta \left\{ \frac{u}{n} \right\} \quad ,$$

$$W_{131} = \frac{1}{2} S_{II} = -\frac{1}{2} \sum ABy \Delta \left\{ \frac{u}{n} \right\} \quad ,$$

$$W_{222} = \frac{1}{2} S_{III} = -\frac{1}{2} \sum B^2 y \Delta \left\{ \frac{u}{n} \right\} \quad , \tag{6}$$

$$W_{220} = \frac{1}{4} S_{IV} = -\frac{1}{4} L^2 \sum C \Delta \left\{ \frac{1}{n} \right\} \quad ,$$

$$W_{311} = \frac{1}{2} S_V = -\frac{1}{2} \sum \frac{B}{A} \left[CL^2 \Delta \left\{ \frac{1}{n} \right\} - B^2 y \Delta \left\{ \frac{u}{n} \right\} \right] \quad ,$$

where $A = ni = n(u + yC)$, $B = n\bar{i} = n(\bar{u} + \bar{y}C)$, $\Delta \left\{ \frac{u}{n} \right\} = \left[\frac{u'}{n'} - \frac{u}{n} \right]$, $L = n(\bar{u}y - u\bar{y})$,

n is the refractive index before the surface, u is the gradient of the ray before the surface, y is the radial distance from the optical axis, and L is the Lagrange Invariant [14]–[16].

1.3 Aberrations in integral imaging

As mentioned previously, spherical aberration makes the marginal rays focus before the paraxial rays (along the optical axis), as shown in Fig. 9(a). Thus, in integral imaging a single object point is imaged as a distorted or blurred volume instead of a 3D image point. Figure 9(b) illustrates how spherical aberration reduces the image resolution and affects the image depth. Aberrations such as coma and astigmatism mostly affect the off-axis viewing characteristics of the InIm, hence influencing the viewing angle of the InIm system.

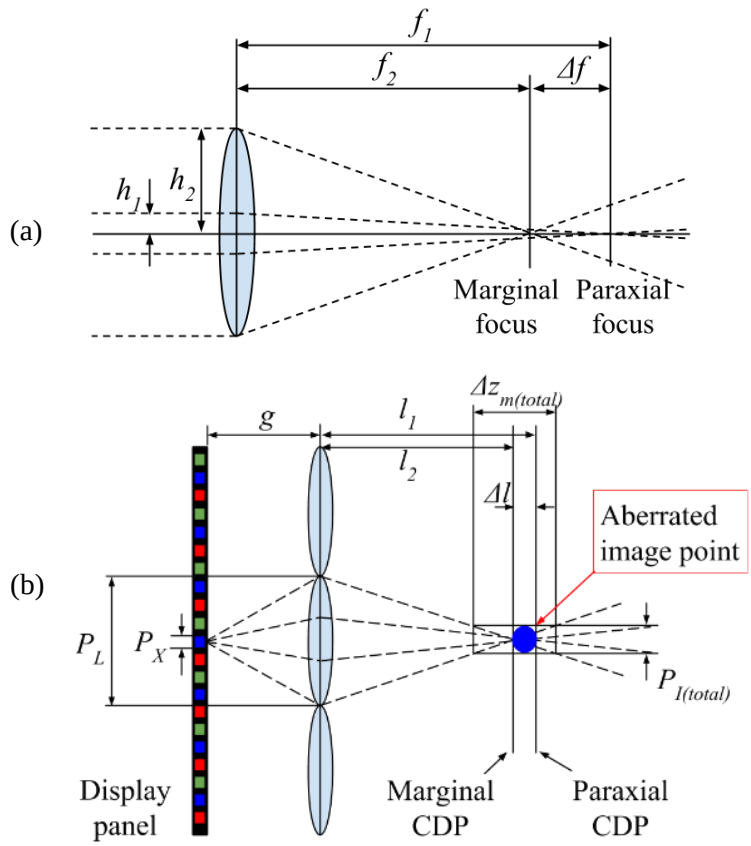

Figure 9: Diagram representation of (a) spherical aberration and (b) aberrated image resolution and image depth in InIm.

The difference in focal length, Δf, is also called longitudinal spherical aberration (LSA) and it causes the central depth plane (CDP) to have a finite thickness, Δl. In fact due to other aberrations the image plane becomes a distorted volume instead of a plane located at distance l from the lens-array. Figure 10 shows the extent at which the image plane is distorted due to spherical aberration, and Eqs. (7) define the parameters of the diagram, where TSA is the transverse spherical aberration and PLC is the width of the point of least confusion.

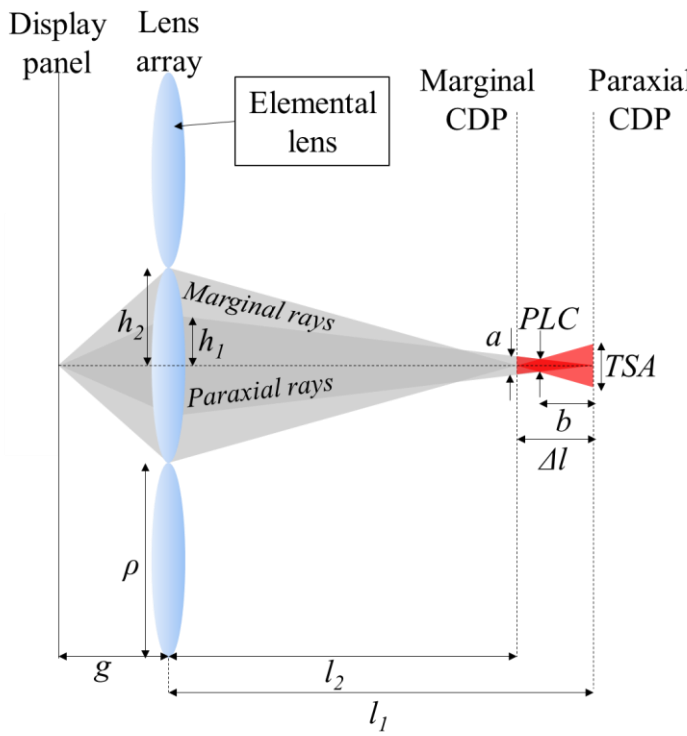

Figure 10: Distorted image plane.

$$a = \frac{2\Delta l h_1}{l_1} \quad ,$$

$$TSA = \frac{2\Delta l h_2}{l_2} = \frac{\Delta l \rho}{l_2} \quad , \tag{7}$$

$$PLC = \frac{aTSA}{a + TSA} \quad ,$$

$$b = \frac{a\Delta l}{a + TSA} \quad .$$

In terms of image quality, Fig. 11 compares the quality of an image (letters S,N, and U) imaged by a single lens with and without spherical aberration. The simulations were performed using LightTools [22] and the image was placed at a distance of twice the lens' focal length. Figure 12 illustrates what effect aberrations

have on the quality of the integrated image in InIm on-axis and off-axis. Computer generated EIs were used for these InIm simulations (virtual mode). These simulations were also performed in LightTools.

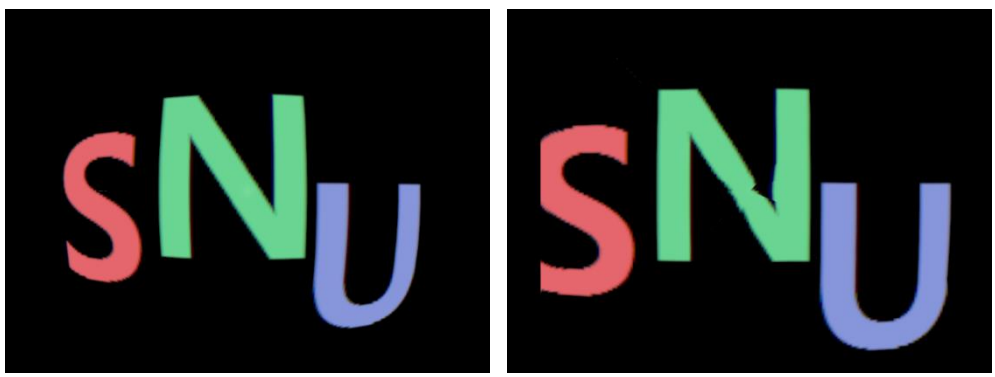

(a) (b)

Figure 11: Distortion caused by (a) a conventional spherical lens and (b) an aspherical lens with reduced spherical aberration. The artifact in the center of (b) is an error by the simulation software.

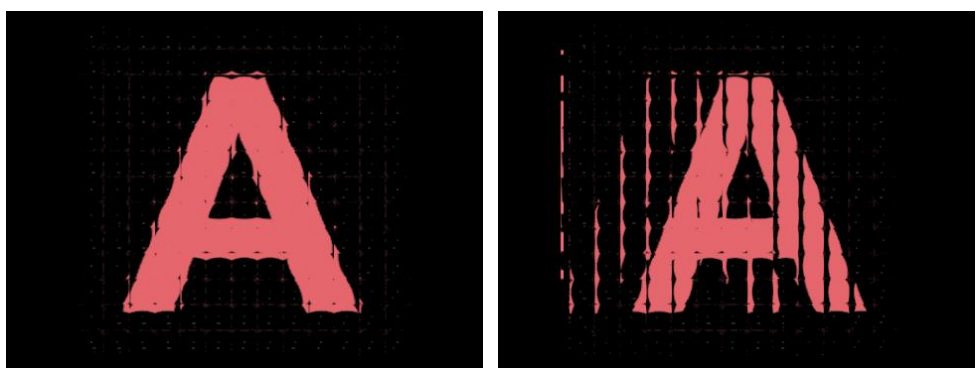

(a) (b)

Figure 12: Distortions in real mode InIm when a conventional spherical lens-array is used. Aberrations affect both (a) on-axis and (b) off-axis views of the reconstructed image. Figures are exaggerated.

1.4 Related work

Due to the disadvantages of InIm there has been a lot of research on improving its resolution and viewing angle [5], [6]. However, not much research has been done addressing the aberrations problem on lens-arrays. Karimzadeh designed a triplet lens-array system for InIm use with aberration consideration [17], though the design method was not specified and there were no simulations or experimental results. In this thesis, the author provides a detailed design method as well as imaging simulations.

Another research group developed a method to design aspherical lens by using numerical analysis [18]. The method uses numerical ray tracing and back-tracing to estimate the ideal aspherical lens surface profile. In this thesis, the author took a similar approach for the second proposed method and applied it to InIm.

1.5 Applications

Having an aberration-free lens-array is ideal not only as a replacement for the conventional lens-array used in InIm but also in other light field applications, such as integral floating display. Integral floating display is a floating display technique which uses the InIm to generate the 3D images and a large floating lens to float the 3D image [19]. Therefore the aberrations present in the InIm system are then magnified by the floating lens, worsening the image quality. In addition to that, if the floating lens is not aberration-corrected either, the aberrations add up and the floated image could become severely distorted.

Lens-array holographic optical element (LA HOE) is a holographic technique that records the optical properties of a lens-array on a transparent photopolymer

which if illuminated with an EI will integrate the 3D image by diffraction [20]. This is a very powerful technique because it can control the pitch of the recorded LA HOE, hence an aberration-free lens-array of large pitch, which is easier to manufacture, could be recorded into a small pitch aberration-free transparent LA HOE.

2 PROPOSED METHODS FOR DESIGNING ABERRATION-MINIMIZED ELEMENTAL LENS

The author chose to design a lens-array with 13 by 13 elements, pitch of 10 mm and made of Poly(methyl methacrylate) (PMMA) (n = 1.49 at 550 nm). The designed lens-arrays are compared to a conventional spherical lens-array of same specification. The chosen elemental lens pitch is slightly large, sometimes referred to as coarse integral imaging [21], but it was selected because it will facilitate the visualization of the optimization result. Manufacturing limitations was another reason for the choice of lens pitch.

2.1 Aberration balancing: Splitting and bending

The aberrations of a single lens can change depending on its size, thickness and shape. Thus lens bending, which is the change of the radius of curvature of the lens, can be used to minimize some aberrations in a singlet. However the minimum aberration achievable with a singlet is still large. Also, realistically a singlet can be made such that it suffers less from one type of aberration, but it cannot eliminate all at the same time. For that more than one lens are required such that the aberrations from one (or more) surface(s) can be compensated by the aberration in other surface(s). This is called aberration balancing [14].

Lens design and optimization

The author's objective was to design a lens system for InIm composed of four lens-array sheets (quartet lens-array) making sure that each channel, i.e.: the elemental lens, had minimum aberration. The author started the design of the elemental lens

from a double convex singlet whose radii of curvature were calculated using the Lens Maker's formula, Eq. (8).

$$\frac{1}{f} = \phi = (n-1)\left(\frac{1}{R_1} - \frac{1}{R_2}\right), \tag{8}$$

where n is the refractive index of the lens medium, f is the focal length, ϕ is the lens's power, and R_1 and R_2 are the radii of curvature of the first and second convex surfaces, respectively. For a desired focal length of 40 mm and refractive index of 1.49, the radii R_1 and R_2 should be 39.2 mm. The singlet was then split into three identical lenses with a combined focal length of 40 mm. Thus the lens's power was divided by three for each lens. Due to the fact that double convex lens-arrays are very difficult to fabricate, two of the six surfaces were flattened. This changed the focal length of the lens so, with the aid of the lens design software Zemax, bending was used to restore the original value of 40 mm. The configuration chosen was based on the Cooke triplet which is a known lens system used in photography. The four convex surfaces were set as variables and optimization was done. The middle concave-convex lens can be split into two and the final design can be achieved. All lenses are 2 mm thick and the lens pitch is 10 mm. There is no spacing between lens 2 and 3, but other lenses are separated by 1 mm. Figure 13 illustrates the design process and Fig. 14 shows the design specifications.

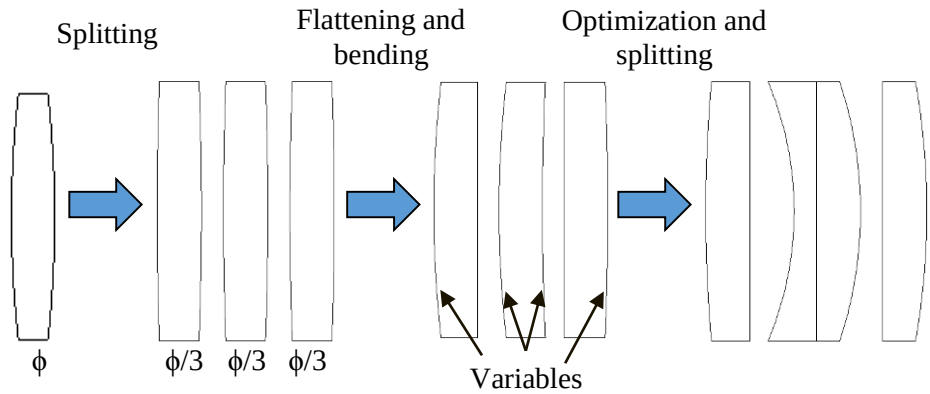

Figure 13: Summary of the design process to achieve a quartet elemental lens with minimum aberrations.

Surf:Type		Comment	Radius		Thickness		Glass		Semi-Diameter	
OBJ	Standard		Infinity		Infinity				Infinity	
*	Standard		48.070	V	2.000		PMMA		5.000	U
2*	Standard		Infinity		2.000				5.000	U
3*	Standard		-11.161	V	1.000		PMMA		5.000	U
4*	Standard		Infinity		0.000				5.000	U
5*	Standard		Infinity		2.000		PMMA		5.000	U
6*	Standard		-13.782	V	1.000				5.000	U
7*	Standard		Infinity		2.000		PMMA		5.000	U
8*	Standard		-24.675	V	40.996	M			5.000	U
IMA	Standard		Infinity		-				3.489	

Figure 14: Designed quartet specifications.

Lens assessment

The designed lens was assessed for aberrations and imaging simulations were carried out. Figure 15 shows how the designed quartet elemental lens behaves under parallel illumination at 0 and 5° compared to the initial singlet. Table 1 shows numerically that the designed quartet elemental lens suffers significantly less from all the main aberrations apart from distortion, though the value is still low and within the acceptable limits.

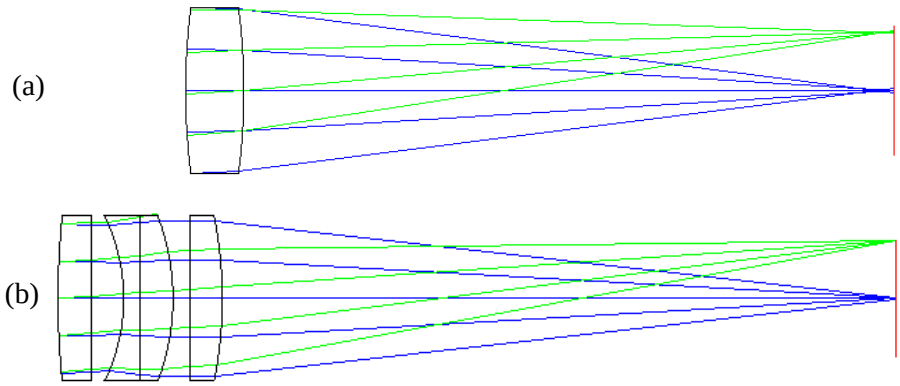

Figure 15: Ray focusing under 0° (blue rays) and 5° (green rays) illumination for the (a) initial singlet and the (b) designed quartet lens.

Table 1: Comparison of the aberration coefficients of the singlet and quartet lens (unit is λ).

	Spherical	**Coma**	**Astigmatism**	**Field curvature**	**Distortion**
Singlet	7.01	-8.10	4.30	1.47	-0.28
Quartet	0.35	0.83	0.98	1.03	1.24

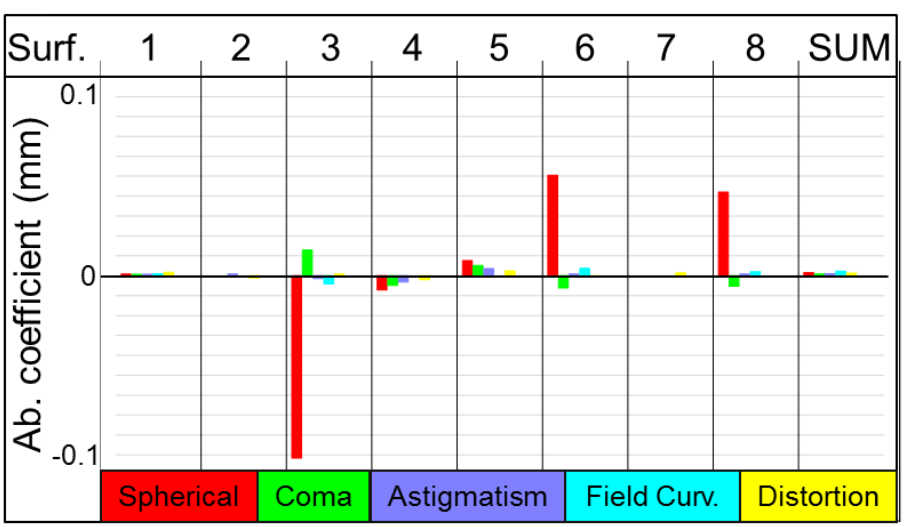

Figure 16: Graphic visualization of the aberration coefficients.

Figure 16 is a graphic representation of the aberration coefficients at each surface of the quartet lens. It is possible to see how the aberrations are being balanced, for example surface 3, which has very high negative spherical aberration due to its strong concave surface shape, is compensated by the positive spherical aberration in surfaces 6 and 8. The modulation transfer function (MTF) plot in Fig. 17 shows that the designed elemental lens works close to the diffraction limit. Figure 18 shows the transverse ray fan plots of the quartet. The ray fan plot is the plot of a ray's pupil position vs. its image plane position relative to the chief ray position in the image plane [14].

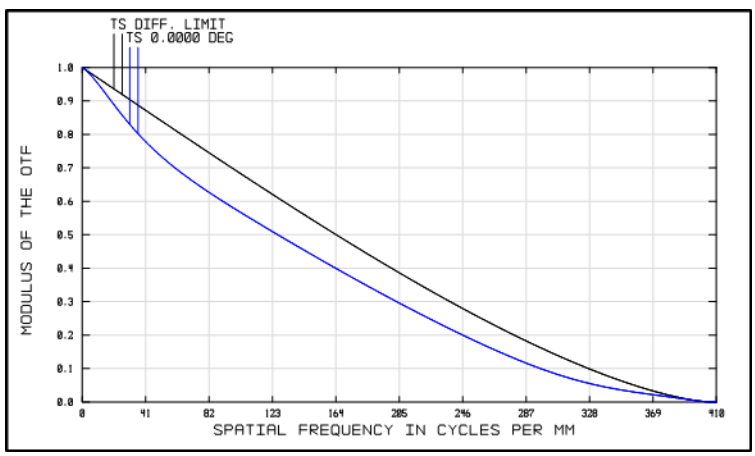

Figure 17: MTF plot shows that the lens works close to the diffraction limit. In the plot, the black line represents the diffraction limit and the blue line represents the performance of the designed lens.

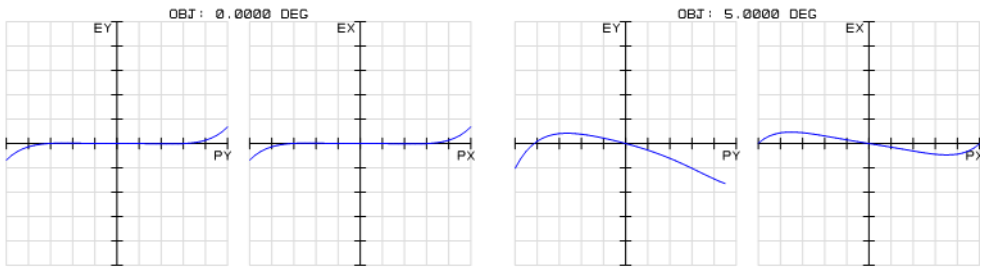

(a) (b)

Figure 18: Transverse ray fan plots show very low aberrations at (a) 0 and (b) 5°. The scale is 100 µm.

The transverse aberrations of the system are very small. There is almost no aberrations present on axis, Fig. 18 (a), but at 5° a small amount of spherical aberration and coma are present but the aberrations are less than 20 µm.

Simulations

Imaging simulations for InIm are performed to test the designed lens array and to demonstrate the effectiveness of the proposed method.

(a)

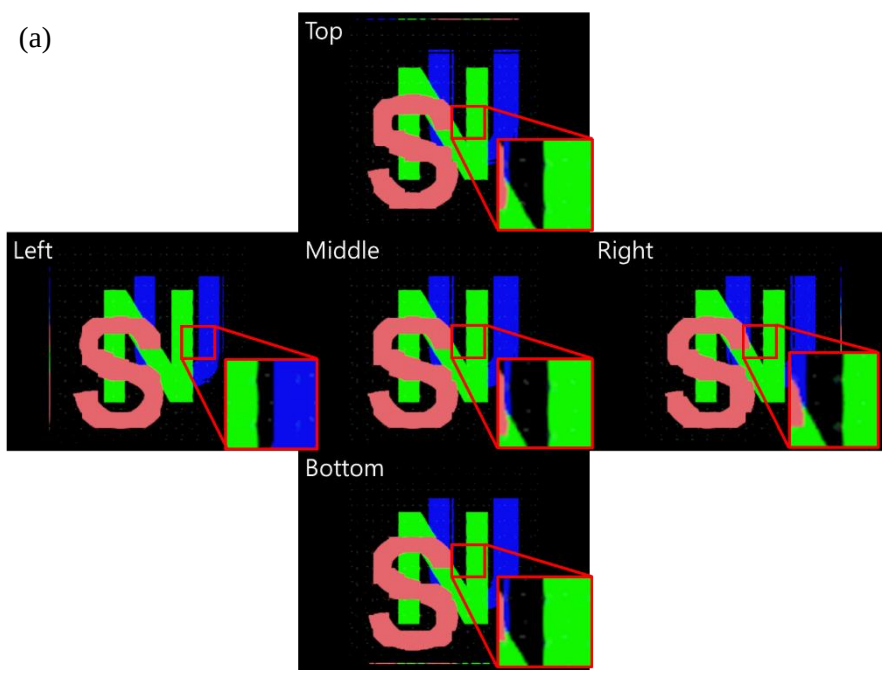

(b)

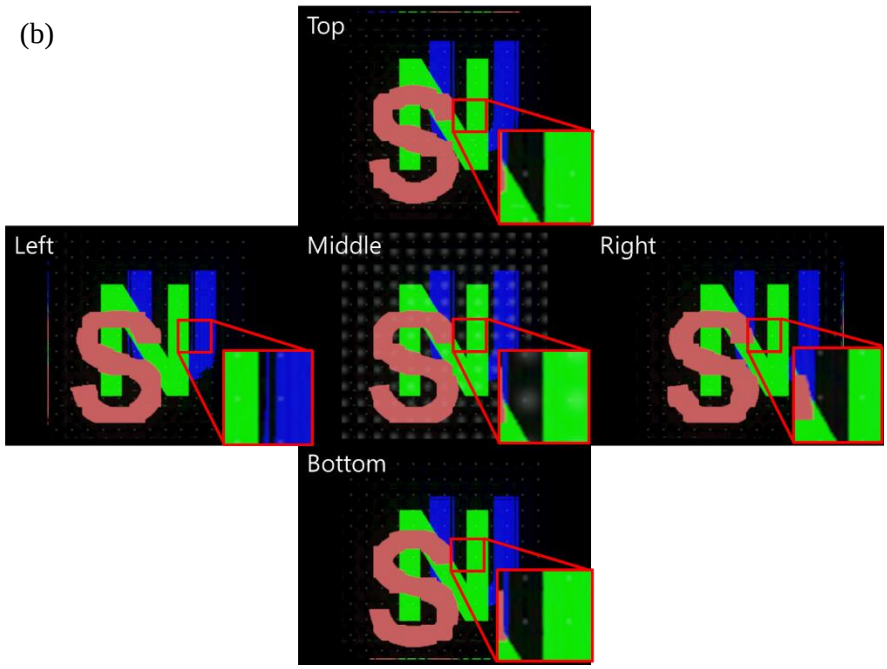

Figure 19: Integral imaging simulations using (a) conventional spherical lens-array and (b) the designed quartet lens-array. The white marks on the middle figure are due to reflections from the virtual light source in the simulation.

Figure 19 shows the results of the integral imaging simulations performed using LightTools [22]. The simulation was performed for virtual mode, the gap was set to 12.5 mm, such that the central depth plane (CDP) was located at 18.2 mm. The objects (letters S, N and U) were separated by 10 mm. The camera was placed 1500 mm away from the lens-array and the perspectives were recorded at angles of -5°, 0° and 5° vertically and horizontally. It is possible to see that for different perspectives the object in focus (letter N) stays sharp and the parallax can be observed for the other letters.

2.2 Numerical ray tracing

For this second method it was desired to design a lens-array of which elemental lens are singlets. This is desirable because it makes the optical system thinner and also removes the calibration and alignment issues present with the quartet lens-array. However, a single lens can be made with an aspherical surface such that it suffers less from one (or two) type(s) of aberration, but it cannot eliminate all at the same time. With that in mind, it is necessary to find the dominant aberration and focus on minimizing it.

For this part of the work, the author chose to design a lens-array with same dimensions as the previous case (Section 2.1) but with a focal length of 17.3 mm. The radius of curvature of the plano-convex elemental lens is 8.49 mm and an arbitrary thickness of 3.5 mm was selected. The Seidel aberration coefficients of a single lens was calculated using Eq. (6) and it was found that spherical aberration has the highest aberration coefficient, as shown in Table 2.

Table 2: Wavefront aberration values of a conventional spherical lens (unit is λ).

Spherical	**Coma**	**Astigmatism**	**Field curvature**	**Distortion**
64.7	14.5	9.35	3.4	0.23

The most effective way to minimize spherical aberration using a single lens is to use aspherical surfaces. The surface profile of an aspherical lens is not a section of a sphere, like spherical lens, and for that reason it can be made such that it refracts rays uniformly for all positions in the exit pupil. The surface profile of an aspherical lens can be described by Eq. (9):

$$z(y) = \frac{y^2}{R\left(1+\sqrt{1-(1+k)\frac{y^2}{R^2}}\right)} + \sum_{i=1} A_i y^{2+2i}, \qquad (9)$$

where z is the surface sag, y is the radial distance from the optical axis, R is the radius of curvature of the lens, k is the conic constant, and A_i is the aspherical coefficient of ith order. The same equation can also describe a spherical lens when k and A_i are equal to zero.

Lens design

Lens design software have optimization functions which can find the ideal lens shape for many applications, however they work by finding the local minimum. Thus the initial values given to the program are very important. In order to find the initial surface profile of the aspherical lens with minimum spherical aberration, the author devised a numerical ray tracing technique.

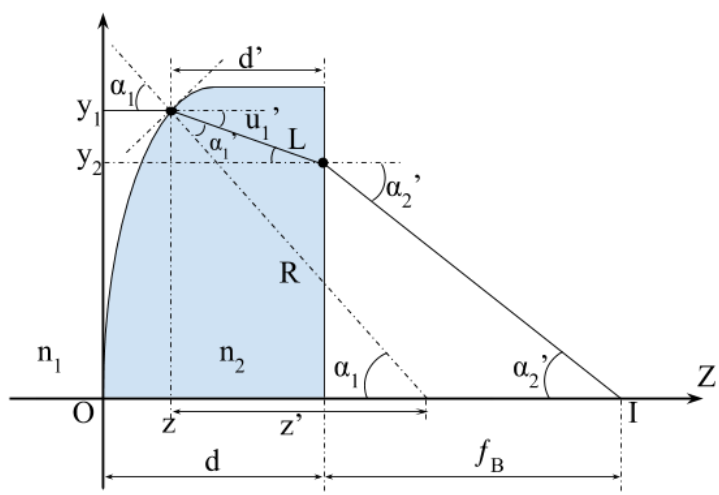

Figure 20: Schematic diagram illustrating the refraction of rays at the surface of the aspherical lens.

In the diagram in Fig. 20, n_1 and n_2 are the refractive indices of the surrounding medium and the lens material, respectively, R is the radius of curvature of the surface 1 at height y, d is the thickness of the lens, f_b is the back focal length and L is the length of the ray path between the two lens' surfaces. Angles α are the angles between the incident ray and the normal to the surface, while angles u are the angles between the incident ray and a line parallel to the optical axis at a radial distance y from the optical axis.

The approach taken was to use Snell's law and trigonometry to obtain equations to trace parallel rays striking the lens at height y_1 until the ray crosses the optical axis at point I. This fulfills the spherical-aberration-free properties because all rays are focusing in the same point. The angle α_2' is chosen to be the system variable such that by varying α_2' over the lens's pitch, the coordinates $(z(\alpha_2'), y(\alpha_2'))$ can be obtained and the surface profile of the lens can be reconstructed. Once the profile is obtained, it is fitted to the aspherical lens equation, Eq. (9), such that the values of R, k and A_i (i = 2,4,6…) are obtained.

Applying Snell's law to the first surface (convex surface), Eq. (10) is obtained:

$$n_1 \sin(\alpha_1) = n_2 \sin(\alpha_1') \quad , \tag{10}$$

where

$$\alpha_1 = \alpha_1' + u_1' \quad . \tag{11}$$

Then in order to find y_2, which is the distance from the optical axis to the height of the ray in surface 2, based on the propagation length L,

$$y_2 = y_1 - L\sin(u_1') \quad . \tag{12}$$

The second refraction can be described by the following equation,

$$n_2 \sin(u_1') = n_1 \sin(\alpha_2') \quad . \tag{13}$$

Note that $\alpha_2' = u_2'$ because the normal to the surface 2 is also parallel to the optical axis. The final equation, Eq. (14), deals with the ray propagation from surface 2 to the focal point *I*.

$$y_2 = f_B \tan(\alpha_2') \, . \tag{14}$$

Equations (10)-(14) are the basic equations used to obtain the functions $y_1(\alpha_2')$ and $z(\alpha_2')$, which define the surface profile in terms of the angle α_2'. Rearranging Eq. (10) and substituting Eq. (11) into (10) we get

$$\frac{n_1}{n_2}\sin(\alpha_1) = \sin(\alpha_1 - u_1') \quad , \tag{15}$$

$$\frac{n_1}{n_2}\sin(\alpha_1) = \sin(\alpha_1)\cos(u_1') - \cos(\alpha_1)\sin(u_1') \quad , \tag{16}$$

$$\frac{n_1}{n_2} = \cos(u_1') - \frac{\sin(u_1')}{\tan(\alpha_1)} \quad . \tag{17}$$

Then,

$$\alpha_1 = \arctan\left[\frac{\sin(u_1')}{\cos(u_1') - n_1 / n_2}\right] \quad . \tag{18}$$

Similarly Eq. (13) can be rewritten as

$$u_1^{'} = \arcsin\left[\frac{n_1}{n_2}\sin(\alpha_2^{'})\right] \quad . \tag{19}$$

Substituting Eq. (14) into Eq. (12) and rearranging for y_1

$$y_1(\alpha_2^{'}) = f_B \tan(\alpha_2^{'}) + L\sin(u_1^{'}) \quad . \tag{20}$$

In order to find L the author uses the assumption that the lens' thickness at the edges is half of that in the middle, in other words $d' = d/2$ when y_1 is at the lens edge. Thus, d' can be approximated as

$$d' \approx d - \left(\frac{\alpha_2^{'}}{\alpha_{\max}}\frac{d}{2}\right), \tag{21}$$

where $\alpha_{\max}$ is the angle caused by the incident ray striking the lens at its edge. Now an expression for L can be written and substituted into Eq. (20), such that

$$L = \frac{d'}{\cos(u_1^{'})} = \left[d - \left(\frac{\alpha_2^{'}}{\alpha_{\max}}\frac{d}{2}\right)\right] \times \frac{1}{\cos(u_1^{'})} \quad , \tag{22}$$

and

$$y_1(\alpha_2^{'}) = f_B \tan(\alpha_2^{'}) + d'\tan(u_1^{'}) \quad . \tag{23}$$

The radius of curvature R is also a function of $\alpha_2^{'}$ and it can be found using the equation

$$R(\alpha_2^{'}) = \frac{y_1(\alpha_2^{'})}{\sin(\alpha_1)} \quad . \tag{24}$$

In the diagram z is defined as the lens sag, which can be defined by the equation

$$z(\alpha_2^{'}) = R(\alpha_2^{'}) - \sqrt{R(\alpha_2^{'})^2 - y_1(\alpha_2^{'})^2} \quad . \tag{25}$$

Equations (20) and (25) are evaluated for all values of $\alpha_2^{'}$ from 0 to $\pm\alpha_{\max}$, where

$$\alpha_{\max} = \arctan\left(\frac{\rho}{2f_B}\right), \tag{26}$$

and ρ is the lens pitch.

Once the profile is obtained it is fitted to the aspherical lens equation, Eq. (9) and the lens parameters were obtained: R = 7.3181, k = -0.6498, A_2 = -0.009.

Optimization

A lens design software was used to optimize the elemental lens. The ray tracing mode used was sequential and the imaging mode was set to focal. The entrance pupil diameter was set to the lens pitch, which is 10 mm. Due to the fact that chromatic aberration is not being considered, a single mid-spectrum wavelength was used for the optimization, which was 550 nm. The object was set at infinity and the glass type chosen was PMMA. The initial values of radius, thickness and conic constant must be set to variable. The author used the Default Merit Function optimizing for root mean square (RMS) spot radius and added specific fields for the aberrations, with a target value of 0. This method produced small spot size and spherical aberration coefficient. Initial results, however, had very large thickness values hence iterations were necessary in order to reduce the thickness of the lens but maintain the performance. The final lens surface profile had radius, R = 8.56 mm and conic constant, k = -0.578. The lens thickness was kept at 3.5 mm. Table 3 and Fig. 21

summarize the design and optimization process, and the effect on the aberrations of the lens.

Lens assessment

The aspherical lens were assessed similarly to the quartet lenses in the previous section.

Table 3: Lens properties at each design stage.

Design stage	Initial spherical lens	Initial aspherical lens	Optimized aspherical lens
Lens properties	R = 8.49 mm k = 0 d_l = 3.5 mm A_i = 0 W_{040} = 64.66 λ	R = 7.32 mm k = -0.6498 d_l = 3.5 mm A_2 = -0.009 W_{040} = 11.62 λ	R = 8.56 mm k = -0.578 d_l = 3.5 mm A_i = 0 W_{040} = -1.51 λ

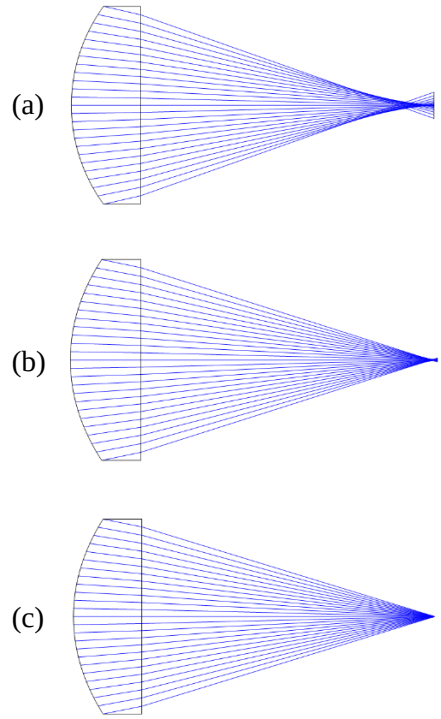

Figure 21: Spherical aberration of the lens at the (a) initial, (b) middle, and (c) final design stages.

As shown in Table 3 and Fig. 21 the spherical aberration coefficient was reduced by almost 50 times. The other aberrations did not change. The initial aspherical lens performs well but it is not optimum because of the approximation used during the derivation of the surface profile equations.

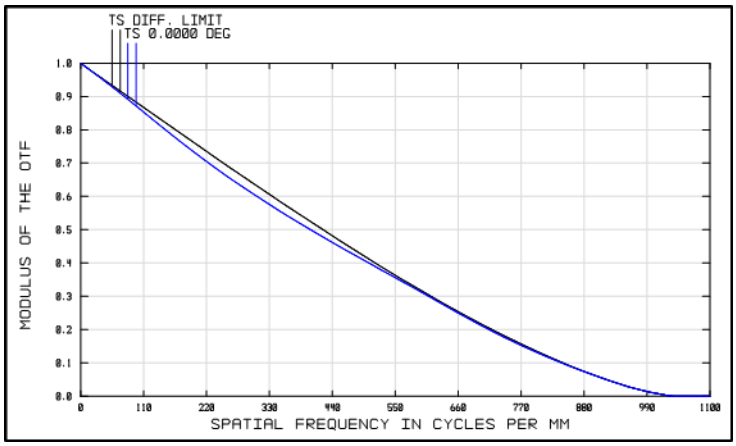

Figure 22: MTF plot shows that the lens works very close to the diffraction limit.

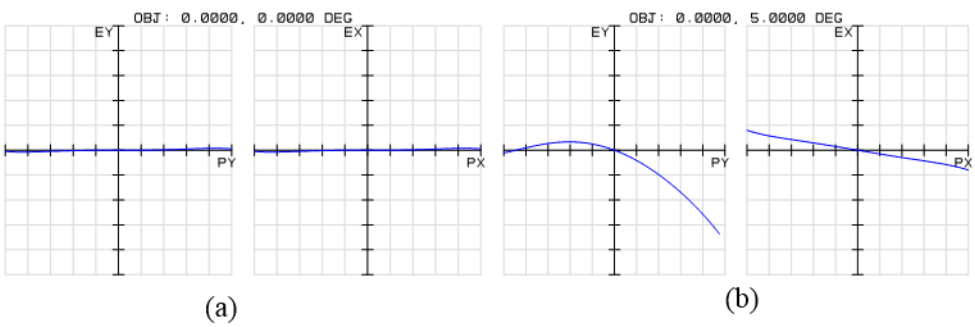

Figure 23: Transverse ray fan plot at (a) 0° and (b) 5° field (scale 200 μm). Spherical aberration has been removed but coma and astigmatism exist for off-axis rays.

Utilizing the analysis tools of the ray tracing software, the plots in Figs. 22 and 23 were obtained. Figure 22 shows the MTF plot of the designed lets, which indicates that the lens works almost at the diffraction limit. The ray fan plots in Figs. 23(a) and (b) show almost zero spherical aberration but significant coma and astigmatism for rays at oblique angles to the optical axis. Comparing the spherical aberration coefficient value with a spherical lens of same properties, shows that the aberration is almost 50 times smaller for the aspherical lens. As mentioned previously the

author focused on minimizing spherical aberration only therefore the other aberrations are the same for both lens: coma, astigmatism, field curvature, and distortion have coefficient values of 14.3, 9.3, 3.4, and 0.2 λ, respectively.

Simulations and experiments

The lens-arrays (one reference spherical and the designed aspherical lens-array) were printed by LUXeXcel using a high precision 3D printer [23]. The tolerances of LUXeXcel's 3D printer are listed in Table 4. Using the printed lens-arrays, spot size and integral imaging experiments were performed and compared to simulations run on LightTools. The results are shown in Figs. 24 and 26.

Table 4: LUXeXcel's printing properties and tolerances.

Material	UV cured PMMA like material
Average deviation (from CAD to printed)	100 micron
Surface roughness	12.5 nm
Minimum element size / pitch	1 mm
Spectral range	420 - 780 nm
Internal transmission 1 mm	99.4%
Haze	0.1%

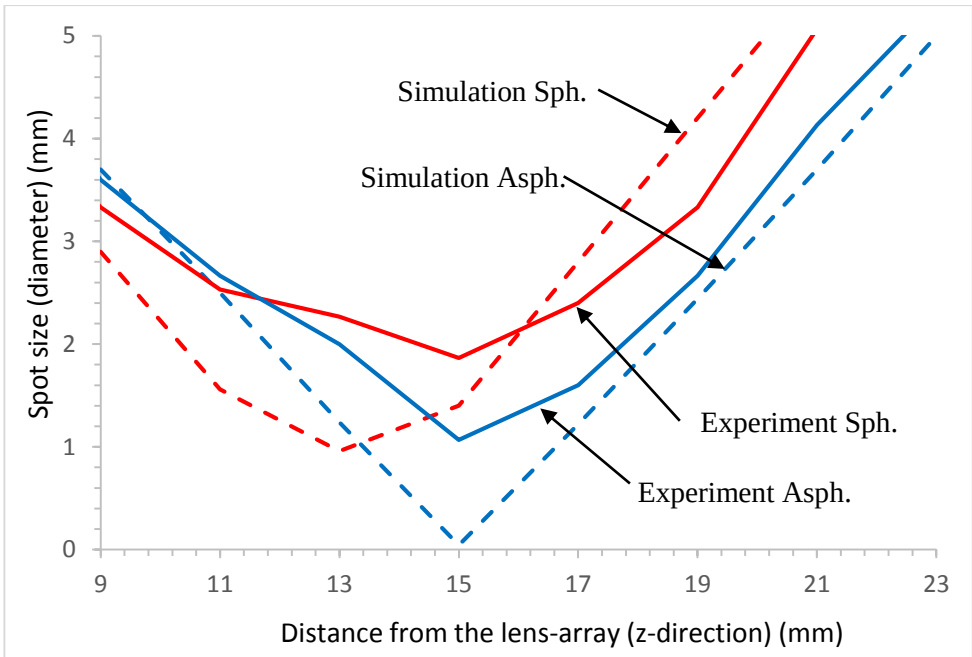

Figure 24: Plot of spot diameter against distance from the lens-array along the optical axis (z-axis).

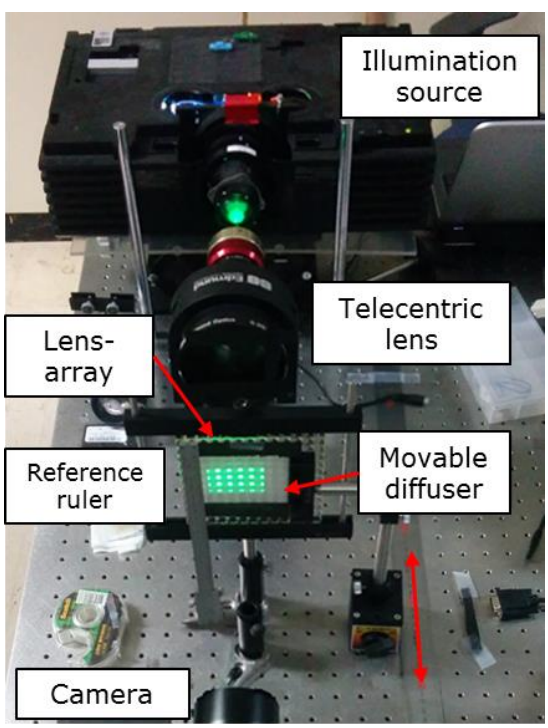

Figure 25: Setup used for the spot size experiment.

The spot diameter experiment was performed using a projector as illumination source, and a telecentric lens was used to make the light beams parallel as they passed through the lens-array. The diffuser was moved along the *z*-direction and the image on the diffuser was recorded by the camera such that the spot patterns of the elemental lens could be retrieved (Fig. 25). With a similar setup, simulations were done and the results are compared in Fig. 24. The experimental results match with the simulations, which predicted that the aspherical elemental lens has a significantly smaller focal spot diameter compared to the spherical elemental lens. The minimum spot size achieved by the aspherical lens was about 1.1 mm compared to 1.9 mm of the spherical lens. It is also possible to see that in all cases the minimum spot size is around $z = 15$ mm, which is the lens's back focal length. The discrepancy between the simulation and experimental values are due to measurement and fabrication errors.

The results of the InIm simulations and experiments are presented in the next chapter.

3 EFFECT OF ABERRATIONS ON THE IMAGE QUALITY OF THE INTEGRAL IMAGING SYSTEM

As discussed in section 1.3, aberrations affect the way each elemental lens images the EI, therefore it affects the way in which the 3D image is integrated. A conventional lens-array has many aberrations which affect the imaging properties in different ways, for example, spherical aberration will mostly affect on-axis viewing, while coma and astigmatism will degrade the image quality if viewed at oblique angles to the screen.

In a perfect case where an aberration-free lens-array is used, a 2D object, for example, would be integrated at the image plane, which in this case is also the CDP. In the case of an aberrated lens-array, the image plane is a distorted volume where the 2D image is reconstructed. So when the image is observed, the viewer sees the 2D image formed on a distorted 3D space, hence the distortion in the viewed image. The same thing happens with a 3D object/image.

The lens-arrays from section 2.2 are used to demonstrate the difference in image quality between an InIm system with aberrated and non-aberrated image planes. Due to the fact that the lens-array used is optimized for spherical aberration, only on-axis images are used. A similar analysis could be done for other aberrations as well.

The results of the InIm experiment (using the setup in Fig. 27) performed for virtual mode are depicted in Figs. 26 (g)-(l) and compared to the simulations, Figs. 26 (a)-(f). The computer generated objects (letters S, N and U) are separated by 10 mm, the central depth plane is at -44.8 mm and the camera was placed 1500 mm from the lens-array. It is clear that the aspherical lens-array performed better than

the spherical one because it removed the unwanted distortions caused by spherical aberration. Both straight and curved lines are less distorted such that the overall image quality is better in the aspherical lens-array experiment.

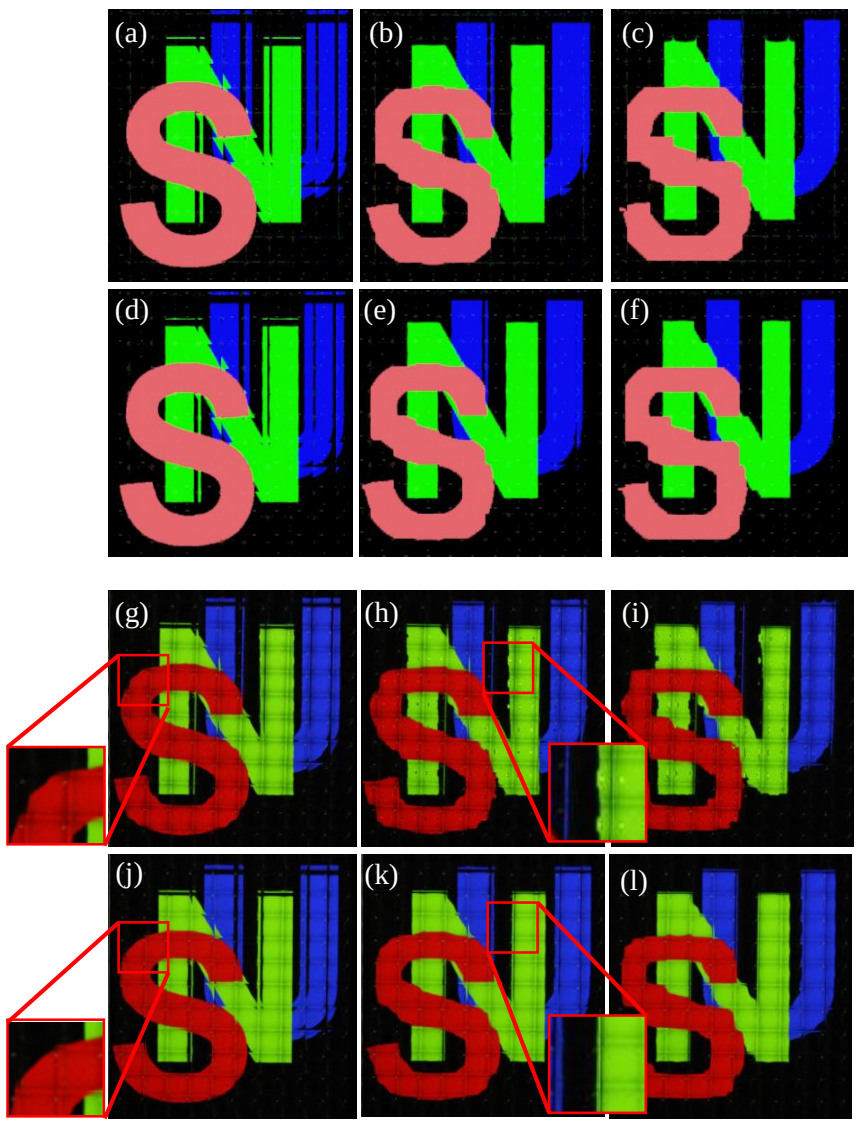

Figure 26: Integral imaging virtual mode (a)-(f) simulations and (g)-(l) experiments. In both cases the top figures are the results of using the spherical lens-array and the aspherical lens-array at the bottom. Also, in the left column figures, (a), (d), (g), and (j), the letter S is in focus, in the middle column

figures the letter N is in focus and in the right column figures the letter U is in focus.

Figure 27: Experimental setup for InIm display.

The author also performed simulations for InIm pickup, using the setup shown in Fig. 29. Figure 28 shows the elemental images recorded using the two lens-arrays. Again it is possible to notice that the aspherical lens-array, Fig. 28(b), performed better because the edges of the cube and cylinder are straight, not distorted like Fig. 28(a).

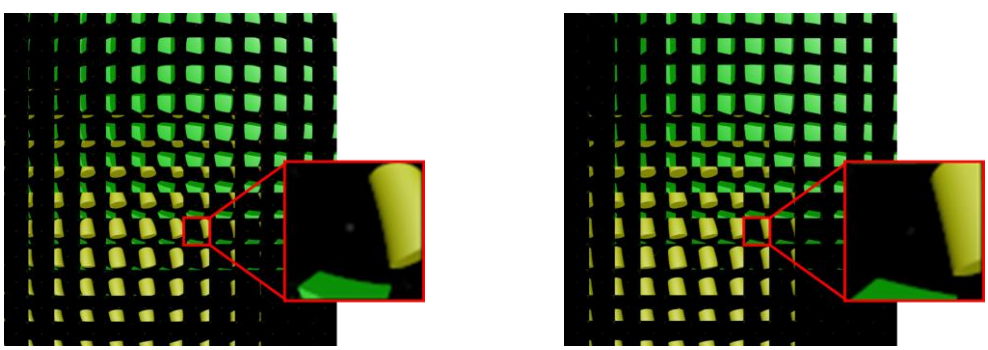

(a) (b)

Figure 28: Simulated integral images recorded using (a) the spherical and (b) the aspherical lens-array.

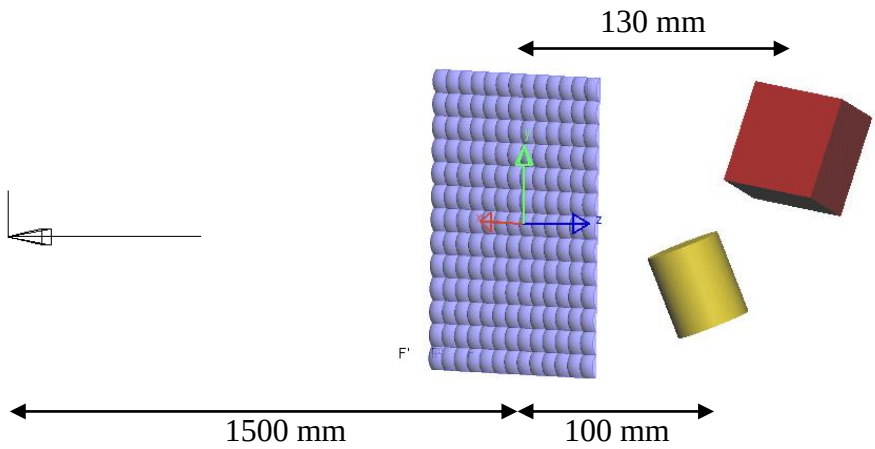

Figure 29: Simulation setup for InIm pickup.

The pickup experiments could not be performed due to some unexpected distortions. Further discussion on this topic is in chapter 5.

4 EFFECT OF ABERRATIONS ON THE VIEWING CHARACTERISTICS OF THE INTEGRAL IMAGING SYSTEM

It was also in the author's interest to analyze how the aberrations affect the viewing characteristics of the InIm system, such as viewing angle and image resolution. The InIm characteristic equations have been defined in the section 1.1.2 and they describe how the 3D image resolution and viewing angle change according to the properties of the InIm system, such as lens pitch and gap. These analysis rely on the assumption that all elemental lenses have perfect imaging characteristics and that the 3D image will be perfectly reconstructed around the paraxial CDP. In reality, due to the lens-array aberrations, the elemental lenses produce aberrated image points, or another way to look at it is that the EIs are imaged on a distorted image plane.

The simultaneous analysis of all the aberrations is too complex, therefore the author will focus on spherical aberration and its effect on the viewing characteristics. As explained previously, spherical aberration causes the marginal rays to focus before the paraxial rays along the optical axis. This is the longitudinal spherical aberration which the author will refer to as the focal error range, Δf. Similarly, if the object is not at infinity the CDP error range, Δl, occurs. On the transverse plane, transverse spherical aberration (TSA) causes the image to be broader and blurred.

As explained in section 1.1.2, the image resolution is a function of the gap, the display resolution, and the imaging distance, therefore if l_1 is considered as the reference imaging distance (ideal case) then Δl is the deviation from that ideal value. Thus by calculating P_{I1} as the ideal image pixel size, and P_{I2} as the maximum

aberrated image pixel size, the ΔP_I can be found (which will be also referred to as $P_{I(ab)}$). In other words $P_{I(ab)}$ is the increase in image pixel size due to spherical aberration. The corresponding values for the image depth Δz_m can be derived from the image pixel size and imaging distance, as per Eq. (3).

Similarly, the viewing angle is a function of the focal length of the lens, hence by finding the ideal focal length f_1 and the maximum aberrated focal length f_2, the values for θ_1 and θ_2 can be obtained, and consequently $\theta_{(ab)}$ which is the decrease in the viewing angle due to spherical aberration. Eqs. (27) summarize what was described above.

$$\begin{aligned} P_{I(total)} &= P_I - P_{I(ab)}, \\ \Delta z_{m(total)} &= \frac{2l}{\rho} P_{I(total)}, \\ \theta_{total} &= \theta - \theta_{ab}. \end{aligned} \tag{27}$$

In order to calculate the values of focal length and imaging distance accurately the use of paraxial calculations are not acceptable because they assume the paraxial approximation $\sin\theta \approx \theta$. This implies that all rays striking any part of the lens will focus on the paraxial focus. An acceptable approximation uses third-order theory. Starting from the third-order equation for the refraction of a ray of light on a single surface [15],

$$\frac{n_1}{s_o} + \frac{n_2}{s_i} = \frac{n_2 - n_1}{R} + h^2 \left[\frac{n_1}{2s_o} \left(\frac{1}{s_o} + \frac{1}{R} \right)^2 + \frac{n_2}{2s_i} \left(\frac{1}{R} - \frac{1}{s_i} \right)^2 \right], \tag{28}$$

where, R is the radius of curvature of the refractive surface, h is the radial distance between the light ray and the optical axis, s_o is the object distance, s_i is the image distance, n_1 is the refractive index before the lens surface, and n_2 is the refractive

index after the lens surface. The image of the refraction on the first surface, Eq. (28), is used as the object for the second refraction. Using a similar equation to Eq. (28) for the second refraction and combining them, the author obtained third-order equations which can be used to find the focusing properties of any spherical or aspherical lens, based on the lens properties. Equations (29) and (30) are used when the object is at infinity, so the back focal length of the lens can be found for a specific ray height.

$$s^3\left(\frac{n-1}{R}\right)+s^2\left(\frac{nh^2}{2R^2}-n\right)-s\left(\frac{nh^2}{R}\right)+\frac{nh^2}{2}=0\,, \tag{29}$$

$$f^3\left[\frac{2(n-1)}{R}+\frac{nh^2}{sR}-\frac{2nh^2}{s^2R}\right]+2f^2-nh^2=0\,. \tag{30}$$

The same applies for Eqs. (31) and (32), but for the case when the object is not at infinity, hence these equations can be used to calculate the imaging plane, or CDP.

$$s^3\left(\frac{1}{g}-\frac{h^2}{2g^3}\right)+ns^2-\frac{nh^2}{2}=0\,, \tag{31}$$

$$l^3\left[\frac{n}{s}-\frac{1-n}{R}-\frac{nh^2}{2s}\left(\frac{1}{s}+\frac{1}{R}\right)^2\right]-l^2\left(\frac{nh^2}{2R^2}-1\right)+l\frac{nh^2}{R}-\frac{nh^2}{2}=0\,, \tag{32}$$

where, s is the location of the image generated by the first refractive surface. It is important to point out that aspherical lens has varying radius of curvature with respect to h, i.e.: $R(h)$, hence it is important to find the R for every radial height using Eq. (24) in the method described in section 2.2. The author used the spherical and aspherical lens-arrays from section 2.2 as examples to demonstrate the difference in

viewing parameters between lens-arrays with high and low aberrations. Using the Eqs. (27)-(32) with the parameters listed in Table 5, the graphs in Figs. 30 and 31 were obtained.

Table 5: Parameters used for the viewing characteristics calculations.

Parameter	**Value**
Display pixel size, P_x	0.1534 mm
Gap, g	12.5 mm
CDP position, l	-44.85 mm
Number of elemental lens, N	9
Refractive index of lens, n	1.49
Lens pitch, ρ	10 mm
Paraxial height, h_1	0.5 mm
Marginal height, h_2	5 mm

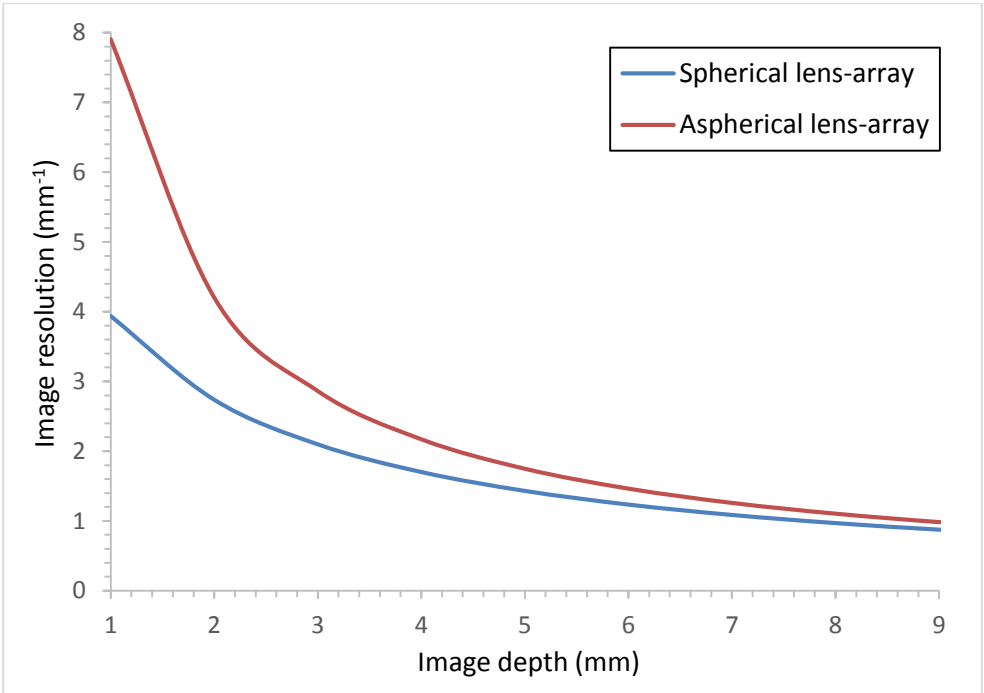

Figure 30: Calculated image resolution against image depth for virtual mode.

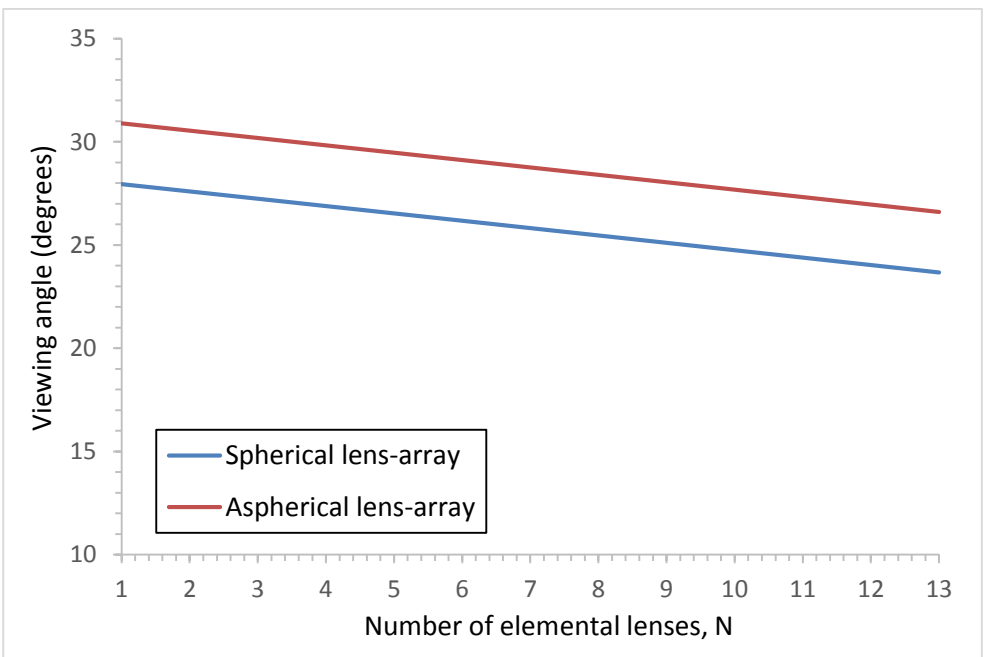

Figure 31: Calculated viewing angle vs. number of elemental lenses involved in displaying the image for virtual mode.

It is possible to see from both graphs that the aspherical lens-array performs better than the spherical lens-array under the same conditions. The difference in image resolution is more significant at small image depths. The InIm in virtual mode from section 2.2 has a calculated image depth of 4.9 mm, and at this depth the resolution of the spherical system is 1.43 mm^{-1} compared to 1.75 mm^{-1} of the aspherical system. Image depth and resolution are very difficult to obtain experimentally, and due to the manufacturing errors (refer to chapter 5) the author decided not to perform the experiments.

The difference in viewing angle between spherical and aspherical systems is fixed at around 3°. Again based on the system used in section 2.2, the number of elemental lenses was 13 and calculated viewing angles were 25.1° and 28°, respectively. The viewing angle experiments agreed with calculations, revealed that the aspherical lens-array was again superior to the spherical one, having viewing angles of 23° and 21°, respectively. The discrepancy is probably due to the errors in the lens-array manufacturing as discussed in chapter 5.

5 DISCUSSION

As mentioned previously the author has encountered some unexpected distortions when trying to record the elemental images using the printed lens-arrays. A similar problem occurred while displaying images in real mode. The company which manufactured the lens-array (LUXeXcel) was contacted and they provided the 3D scan data of the printed lens-arrays. As shown in Fig. 32 the deviation from the design specification to the printed shape is as high as -566 µm in the *z*-direction (height). This deviation is especially severe in the center part of the elemental lens located in the middle of the lens-array. As a result of the deviations, the elemental lenses are flattened in the center which essentially creates a second focal length, as shown in Fig. 33. The virtual mode experiments could still be realized and the difference between the spherical and aspherical lenses could be noticed because the printing of the edge region of the lenses was more accurate than the center region. Therefore at short gap the EIs could still be integrated properly.

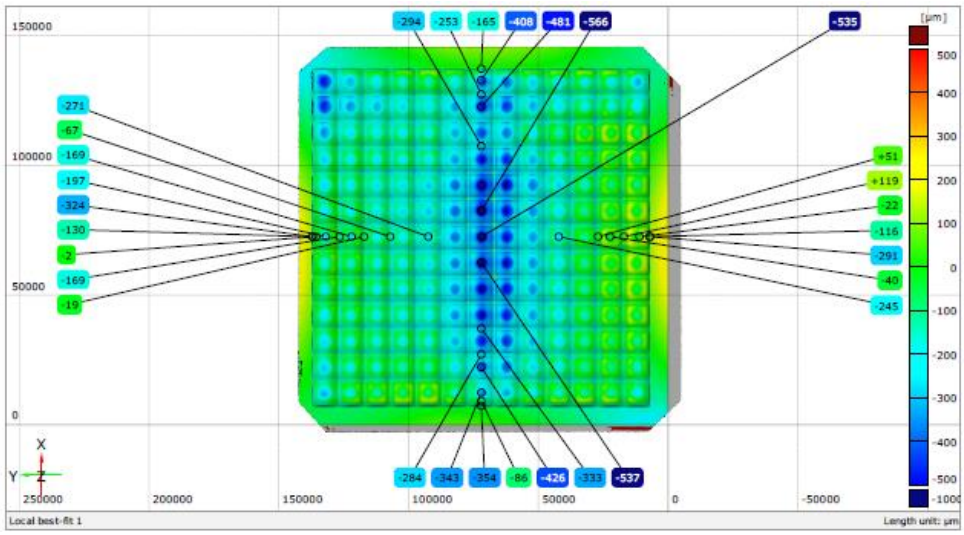

Figure 32: 3D scan data of the printed aspherical lens-array. The scale provided on the diagram represents the deviation, in micrometers, of the printed shape from the design specifications (CAD file) in the *z*-direction. Negative values mean that the printed shape is lower than it should be.

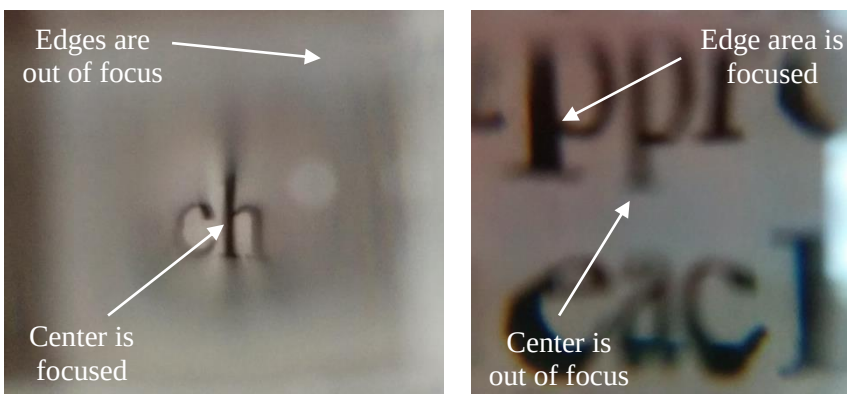

Figure 33: Imaging problem of a single printed elemental lens.

LUXeXcel uses a patented 3D printing technique called printoptical which works by depositing layers of UV-curable polymer on a substrate and applying UV light to harden the material, as illustrated in Fig. 34. Smooth optical surfaces are achieved by using a high resolution print tip and delaying the curing process such

that the layers flow and fuse together [24]. This technique has many advantages over other lens manufacturing methods such as invariance to shape complexity, speed and cost. The author believes this technology is more appropriate for lighting purposes such as light emitting diode (LED) lens and not accurate enough for imaging applications.

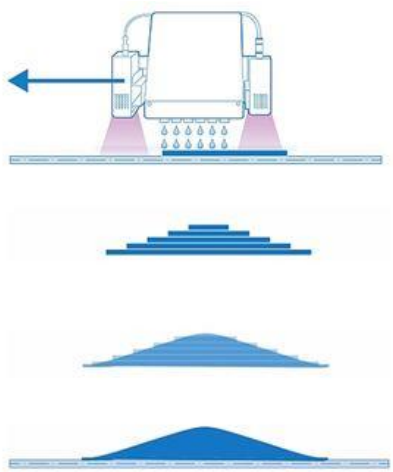

Figure 34: PrintOptical technology used by LUXeXcel.

Despite its many advantages, 3D printing of optical components is still not as accurate as it needs to be for imaging applications. Therefore in our case, a solution to our problem would be using a more trusted and refined printing technique such as injection molding and diamond turning [25].

6 CONCLUSION

In this work the author proposes two simple methods to design, optimize and test an aspherical lens-array that has minimum spherical aberration and a quartet lens-array that is optimized for most monochromatic aberrations. The author also demonstrates by the means of simulations and experiments that compared to a conventional spherical lens-array, the proposed lens-arrays improve the quality of the recorded elemental images and integrated 3D image of the InIm system.

The author also analyzes the degradation of the viewing properties of the InIm system caused by aberrations. The spherical and aspherical lens-arrays were used as examples to quantify the loss in image resolution and viewing angle due to spherical aberration.

BIBLIOGRAPHY

[1] J. Hong, Y. Kim, H.-J. Choi, J. Hahn, J.-H. Park, H. Kim, S.-W. Min, N. Chen, and B. Lee, "Three-dimensional display technologies of recent interest: principles, status, and issues," *Appl. Opt.* **50**(34), p. H87 (2011).

[2] J.-H. Park, K. Hong, and B. Lee, "Recent progress in three-dimensional information processing based on integral imaging," *Appl. Opt.* **48**(34), pp. H77–H94 (2009).

[3] Y. Kim, K. Hong, and B. Lee, "Recent researches based on integral imaging display method," *3D Res.* **1**, pp. 17–27 (2010).

[4] G. Lippmann, "La Photographic Integrale," *C. R. Acad. Sci.* **146**(9), pp. 446–451 (1908).

[5] J.-S. Jang and B. Javidi, "Improved viewing resolution of three-dimensional integral imaging by use of nonstationary micro-optics," *Opt. Lett.* **27**(5), pp. 324–326 (2002).

[6] J.-S. Jang and B. Javidi, "Improvement of viewing angle in integral imaging by use of moving lenslet arrays with low fill factor," *Appl. Opt.* **42**(11), pp. 1996–2002 (2003).

[7] Lytro, https://www.lytro.com/.

[8] M. Hirsch, D. Lanman, H. Holtzman, and R. Raskar, "BiDi Screen: a thin, depth-sensing LCD for 3D interactions using light fields," *ACM Trans. Graph.* **28**(5), pp. 159:1–159:9 (2009).

[9] R. Martínez-Cuenca, G. Saavedra, M. Martínez-Corral, and B. Javidi, "Progress in 3-D multiperspective display by integral imaging," *Proc. IEEE* **97**(6), pp. 1067–1077 (2009).

[10] J. Arai, H. Kawai, and F. Okano, "Microlens arrays for integral imaging system," *Appl. Opt.* **45**(36), pp. 9066–9078 (2006).

[11] F. Okano, H. Hoshino, J. Arai, and I. Yuyama, "Real-time pickup method for a three-dimensional image based on integral photography," *Appl. Opt.* **36**(7), pp. 1598–1603 (1997).

[12] S. W. Min, J. Kim, and B. Lee, "New characteristic equation of three-dimensional integral imaging system and its applications," *Japanese J. Appl. Physics, Part 2 Lett.* **44**(2), pp. L71-L74 (2005).

[13] H. Choi, Y. Kim, J. Park, S. Jung, and B. Lee, "Improved analysis on the viewing angle of integral imaging," **44**(12), pp. 2311–2317 (2005).

[14] J. M. Geary, *Introduction to Lens Design* (Willmann-Bell, Inc., 2002).

[15] E. Hecht, *Optics* (Addison Wesley, 2002).

[16] C. Gardner, "Application of the algebraic aberration equations to optical design," *Trans. Opt. Soc.* **22**(27), pp. 73–203 (1925).

[17] A. Karimzadeh, "Integral imaging system optical design with aberrations consideration," *Appl. Opt.* **54**(7), pp. 1765-1769 (2015).

[18] G.-I. Kweon and C.-H. Kim, "Aspherical lens design by using a numerical analysis," *J. Korean Phys. Soc.* **51**(1), p. 93 (2007).

[19] S.-W. Min, M. Hahn, J. Kim, and B. Lee, "Three-dimensional electro-floating display system using an integral imaging method," *Opt. Express* **13**(12), pp. 4358–4369 (2005).

[20] C. Jang, K. Hong, J. Yeom, and B. Lee, "See-through integral imaging display using a resolution and fill factor-enhanced lens-array holographic optical element," *Opt. Express* **22**(23), p. 27958 (2014).

[21] S. Sawada and H. Kakeya, "Coarse integral volumetric imaging with flat screen and wide viewing angle," *J. Electron. Imaging* **21**(1), p. 011004 (2012).

[22] LightTools - Synopsys Optical Solutions, www.optics.synopsys.com/lighttools/.

[23] LUXeXcel - 3D Printed Optics, https://www.luxexcel.com/.

[24] 3D Printing Optics with LUXeXcel - Nanalyze, http://www.nanalyze.com/2013/08/3d-printing-led-optics-with-luxexcel/.

[25] K. Schwertz, "An introduction to the optics manufacturing process," *OptoMechanics Report* (2008).

ABSTRACT IN KOREAN

렌즈 어레이의 수차에 의하여 저하되는 집적 영상의 시야 특성을 향상시키는 렌즈 디자인에 대한 연구

Matheus Farias Miranda
전기 컴퓨터 공학부 (Dept. of Electrical Eng. and Comp. Sci.)
The Graduate School
Seoul National University

집적영상은 편광안경 등의 부가적인 장비 없이 사용자에게 수평 및 수직 시차를 제공하여 삼차원 영상을 구현할 수 있는 유망한 기술이다. 집적영상 시스템에서 요소영상을 집적하여 삼차원 이미지를 나타내기 위해서는 패널로부터 나오는 광선의 방향을 변조하여 줄 수 있는 렌즈어레이가 필수적이다. 기존의 렌즈어레이는 구면렌즈들로 이루어져 있어, 구면 수차와 비점수차와 같은 문제점을 안고 있다. 수차는 렌즈가 빛을 한 점으로 모으지 못하게 하거나 한 점으로부터 나오는 빛을 시준하지 못하게 한다. 집적영상에서 이와 같은 수차는 요소영상을 왜곡시키며, 결국 이는 재생된 영상의 질의 저하로 이어진다. 또한 집적영상의 성능을 결정하는 시야각과 해상도 역시 이러한 수차의 영향을 받는다.

본 연구에서는 렌즈어레이의 수차를 최소화시키기 위한 두가지 설계 방법을 제시한다. 첫번째로 제안된 설계 방법은 렌즈어레이의 각 요소렌즈에 스플리팅과 벤딩 방법을 적용시켜 수차 보정을 수행하는 방법이다. 시뮬레이션을 통해 기존의 구면렌즈와 비교하여 제안된 방법으로 설계한 렌즈의 성능향상을 검증하였다. 두번째로, 최소 구면수차를 가지는 비구면 렌즈어레이의 설계 방법을 제안하였으며, 제안된 렌즈어레이의 설계과정과 최적화, 실제 제작과정에 대하여 기술하였다. 또한 성능평가 및 분석과, 제안된 방법의 이슈에 대한 해결방안을 제시하였다.

주요어 : 집적영상, 렌즈 설계, 수차, 3D 디스플레이
학 번 : 2013-23844